

The equilibrium points and stability of grid-connected synchronverters

Pietro Lorenzetti, Zeev Kustanovich, Shivprasad Shivratri and George Weiss

Abstract—Virtual synchronous machines are inverters with a control algorithm that causes them to behave towards the power grid like synchronous generators. A popular way to realize such inverters are synchronverters. Their control algorithm has evolved over time, but all the different formulations in the literature share the same “basic control algorithm”. We investigate the equilibrium points and the stability of a synchronverter described by this basic algorithm, when connected to an infinite bus. We formulate a fifth order model for a grid-connected synchronverter and derive a necessary and sufficient condition for the existence of equilibrium points. We show that the set of equilibrium points with positive field current is a two-dimensional manifold that can be parametrized by the corresponding pair (P, Q) , where P is the active power and Q is the reactive power. This parametrization has several surprising geometric properties, for instance, the prime mover torque, the power angle and the field current can be seen directly as distances or angles in the (P, Q) plane. In addition, the stable equilibrium points correspond to a subset of a certain angular sector in the (P, Q) plane. Thus, we can predict the stable operating range of a synchronverter from its parameters and from the grid voltage and frequency. Our stability result is based on the intrinsic two time scales property of the system, using tools from singular perturbation theory. We illustrate our theoretical results with two numerical examples.

Index Terms—Virtual synchronous machine, frequency droop, voltage droop, inverter, synchronverter, Park transformation, saturating integrator, singular perturbation method.

I. INTRODUCTION

Most distributed generators are connected to the utility grid via inverters that rely on various control algorithms to maintain synchronism. They usually offer no inertia, and behave as controlled current sources that produce fluctuating power. Numerous researchers are investigating how the future power grids should be controlled when inverters become dominant, offering competing control algorithms for grid-forming converters, see for instance the recent study [28]. One of the proposed approaches is to emulate the behavior of synchronous generators (SG), so that an inverter-based grid behaves like one based on SG, see for instance [4], [7], [9], [16], [19], [23], [28], [31], [36]. This has many advantages, such as backward compatibility with the current grid, well known black start and fault ride-through procedures, and well

tested primary and secondary frequency and voltage support algorithms. Following [4], inverters that behave towards the utility grid like synchronous machines are called *virtual synchronous machines* (VSM).

One particular type of VSM are the *synchronverters*, introduced in [36], [37]. This type of inverter has attracted considerable attention, see for instance [1], [2], [5], [8], [23], [26], [33]–[35], and the recent survey [29]. The hardware of a synchronverter is similar to that of a conventional three phase inverter (with any number of DC levels, most commonly 3), the novelty is in the control algorithm. The only hardware difference is that some fast acting energy storage (typically, capacitors) is required on the DC bus, to provide the energy pulses (both positive and negative) needed for the emulation of rotor inertia. We base our modelling on the simplified circuit diagram of a grid-connected inverter in Fig. 1. Even though the synchronverter control scheme has evolved over time, all the formulations present in the literature share the same “basic control algorithm”. We base our modelling on this basic algorithm (see Fig. 2 in Sect. II for more details).

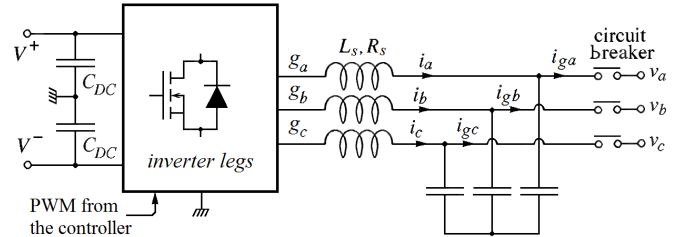


Fig. 1. An inverter with an LC filter receiving DC voltages V^+ , V^- and connected to the grid voltages v_a, v_b, v_c . The control algorithm receives measurements of v_a, v_b, v_c and of the grid currents i_{ga}, i_{gb}, i_{gc} .

The stability of a SG (or VSM) connected to an infinite bus is a well motivated classical problem in the study of power systems. For instance, in [10, Sect. 12.3] and [13] we can find the stability analysis of a linearized second order approximation of this system. The same problem, with a more complex SG model, has been addressed in [24]. In the last decade, motivated by the growing interest in VSM-based grids, similar stability studies have been performed for more complex models of grid-connected VSM. In [3], [20] a fourth order model is formulated for a grid-connected VSM, and conditions on the parameters ensuring almost global asymptotic stability (aGAS) are derived, and in [17] a novel technique for state-space modeling of grid-connected converters is presented, with local stability evaluation via eigenvalues. In [27] a VSM model is developed, which contains a DC side that interacts with the

This research was supported by the Israeli Ministry of Infrastructure, Energy and Water, grant numbers 217-11-037 and 219-11-128. P. Lorenzetti is a team member in the ITN network ConFlex, funded by the European Union’s Horizon 2020 research and innovation program under the Marie Skłodowska-Curie grant agreement no. 765579.

P. Lorenzetti, S. Shivratri and G. Weiss are with the School of Electrical Engineering, Tel Aviv University, Ramat Aviv, Israel (e-mail: shivprasadshivratri8793@gmail.com, plorenzetti@tauex.tau.ac.il, gweiss@tauex.tau.ac.il)

Z. Kustanovich is with the Israel Electricity Company, North District (e-mail: kustanz875@gmail.com, phone: +972-523995779)

AC side in an ingenious way, leading to aGAS of the VSM connected to an infinite bus. In the context of microgrids, stability results are derived in [6], [25], [32], and the importance of accurate modeling has been discussed, among others, in [30] and in the recent review [22]. The paper [18] presents an interesting equilibrium point analysis for microgrids interfaced via solid-state transformers. This analysis is then employed to develop a power sharing algorithm between the inverters.

This paper investigates the local asymptotic stability of a VSM functioning according to the basic synchronverter algorithm, when connected to a powerful grid modelled as an infinite bus. For this purpose, we formulate a fifth order grid-connected synchronverter model. This model is an extension of the fourth order model developed and analyzed in [3], [20], where the rotor (or field) current was assumed to be constant (thus ignoring the reactive power control loop). Using advanced mathematical methods, different sufficient conditions for almost global asymptotic stability of the fourth order model were derived in [3], [20]. Here we include the field current as the fifth state variable and we investigate the stability of the equilibrium points of the resulting fifth order system.

We derive a novel geometric representation of the fourth and fifth order models' equilibrium points. We use extensively the mapping of equilibrium points into the *power plane*, where the coordinates are P (the active power) and Q (the reactive power). (In the language of differential geometry, the manifold of equilibrium points with positive field current is diffeomorphic to the power plane.) We show that, for a fixed prime mover torque and for field current values in a "reasonable" range, the image of the fourth order model equilibrium points in the power plane moves on a circle. The radius of this circle depends on the prime mover torque at the equilibrium. In the same geometric representation, we identify a stability sector for the fifth order model equilibrium points. This sector allows to determine a priori if certain reference values of active and reactive power will generate stable (or unstable) fifth order model equilibrium points.

The paper is organized as follows. In Sect. II we recover the fourth order grid-connected synchronverter model from [20], [21], and we extend it to a fifth order one, adding the field current to the state vector. In Sect. III the equilibrium points of the fourth order model are studied and the novel geometric representation is introduced. In Sect. IV we study the equilibrium points of the fifth order model and their representation in the power plane. In Sect. V we use results from Sect. III and IV to find a sufficient condition ensuring the stability of the fifth order model equilibrium points, employing singular perturbation methods developed in [15]. Based on this result, we characterize the power plane region corresponding to stable fifth order model equilibrium points. Finally, in Sect. VI we use two numerical examples to illustrate our novel geometric representation and our theoretical derivations.

II. MODELLING THE GRID-CONNECTED SYNCHRONVERTER

In this section we construct the basic fifth order model of the synchronverter, following the terminology and notation of

[20], [21], [37]. Note that the paper [21] has proposed five modifications to the synchronverter algorithm from [37], to improve its stability and performance. Of these, we adopt here only the two most important ones: a substantial increase of the effective size of the filter inductors, by using virtual inductors, and the improved anti-windup field current controller.

Our analysis is based on a simplified model of a synchronverter, given in Fig. 2. This model is simplified because it does not take into account the various low-pass filters that are included to reduce high frequency noise, and it also ignores most of the saturation blocks included in the algorithm (see [5], [21]) (however, the saturating integrator contained in the field current controller is considered). We also ignore start-up procedures and various protections. Including these features would result in a high-order model that is practically impossible to analyze rigorously. Moreover, ignoring the aforementioned features does not significantly alter the steady-state behaviour of the system, making our stability analysis relevant also for higher order models.

We proceed as follows: first we recover the fourth order model from [21] (where the field current i_f was assumed to be a parameter). Then, we extend this model by including i_f as a state variable, obtaining a fifth order model.

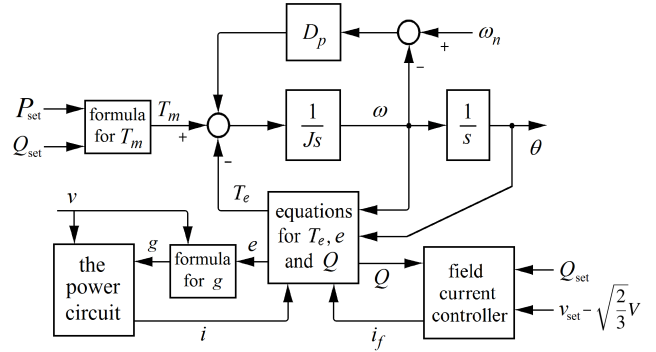


Fig. 2. The simplified block diagram of a synchronverter, adapted from [21, Fig. 2]. The signals v, g, e and i are three dimensional.

We denote by θ_g the grid angle and by ω_g the grid frequency, so that $\omega_g = \dot{\theta}_g$. The frequency ω_g is usually close to $\omega_n = 100\pi$ rad/sec. We denote by θ the synchronverter virtual rotor angle, and by ω its angular velocity, so that $\omega = \dot{\theta}$. The difference $\delta = \theta - \theta_g$ is called the *power angle*. The notation $\widetilde{\cos \theta}$ and $\widetilde{\sin \theta}$ is defined by

$$\begin{aligned} \widetilde{\cos \theta} &= \begin{bmatrix} \cos \theta & \cos \left(\theta - \frac{2\pi}{3} \right) & \cos \left(\theta + \frac{2\pi}{3} \right) \end{bmatrix}^\top, \\ \widetilde{\sin \theta} &= \begin{bmatrix} \sin \theta & \sin \left(\theta - \frac{2\pi}{3} \right) & \sin \left(\theta + \frac{2\pi}{3} \right) \end{bmatrix}^\top. \end{aligned}$$

Then the grid voltage vector is

$$v = \sqrt{\frac{2}{3}} V \widetilde{\sin \theta}_g, \quad (1)$$

where V is a positive constant or a slowly changing signal (this is the rms value of the line voltage).

Denote by $M_f > 0$, the peak mutual inductance between the virtual rotor winding and any one stator winding, by i_f the variable *field current* (or rotor current) and by e the vector

of electromotive forces, also called the *internal synchronous voltage*. We rewrite [37, eq.(4)]:

$$e = M_f i_f \omega \widetilde{\sin \theta} - M_f \frac{di_f}{dt} \widetilde{\cos \theta} \quad (2)$$

and we note that the variable current i_f governs the amplitude of e . We apply the *Park transformation*

$$U(\theta) = \sqrt{\frac{2}{3}} \begin{bmatrix} \cos \theta & \cos(\theta - \frac{2\pi}{3}) & \cos(\theta + \frac{2\pi}{3}) \\ -\sin \theta & -\sin(\theta - \frac{2\pi}{3}) & -\sin(\theta + \frac{2\pi}{3}) \\ 1/\sqrt{2} & 1/\sqrt{2} & 1/\sqrt{2} \end{bmatrix}$$

to (2). For any \mathbb{R}^3 -valued signal v , the first two components of $U(\theta)v$ are called the dq coordinates of v , denoted by v_d, v_q . By using the notation $m = \sqrt{3/2}M_f$, we represent the internal synchronous voltage e in dq coordinates as:

$$e_d = -m \frac{di_f}{dt}, \quad e_q = -mi_f \omega. \quad (3)$$

The term e_d can be neglected, because the rate of change of the field current is small, so that $e_d \ll e_q$. Thus, in the synchronverter algorithm from [37] the approximation $e_d = 0$ is adopted, and our analysis will follow this. (We remark that we did simulation experiments with e_d as in (3), and the results were practically the same as for $e_d = 0$.)

Applying the Park transformation to (1), we get the dq representation of the grid voltage as

$$v_d = -V \sin \delta, \quad v_q = -V \cos \delta. \quad (4)$$

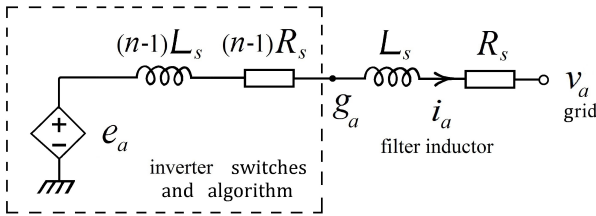


Fig. 3. A synchronverter with filter inductor L_s and its resistance R_s . e_a is the synchronous internal voltage. The inductor and the resistor multiplied with $(n-1)$ are virtual. Only phase a is shown. This is taken from Fig. 4 in [21].

The control algorithm computes $g = [g_a \ g_b \ g_c]^T$ and sends it to the switches in the power part (see Fig. 3). In the original synchronverter algorithm from [37], we have $g_d = e_d$ and $g_q = e_q$, i.e., the internal synchronous voltage e from (2) is sent straight to the PWM signal generator. Here we consider the modified synchronverter equations according to [21], which contain the original algorithm as a special case, namely $n = 1$. Writing [21, eq.(22)] in dq coordinates, we have

$$g_d = \frac{(n-1)v_d + e_d}{n}, \quad g_q = \frac{(n-1)v_q + e_q}{n}.$$

The current sensors are placed after the filter capacitors, as shown in Fig. 1, to avoid the switching noise. From these measurements, the inductor currents i_a, i_b, i_c can be estimated. (Alternatively, in some versions of synchronverters, the output elements L_s and R_s are virtual, e.g., see [11], and then the currents i_a, i_b, i_c are computed in the algorithm from the

voltage measurements.) By applying the Park transformation on the circuit equations corresponding to Fig. 3, we have

$$L_s \frac{di_d}{dt} = -R_s i_d + \omega L_s i_q + g_d - v_d, \quad (5)$$

$$L_s \frac{di_q}{dt} = -\omega L_s i_d - R_s i_q + g_q - v_q. \quad (6)$$

Here, L_s and R_s are positive constants. Combining (3)-(6) (with $e_d = 0$) and using the notation

$$R = nR_s, \quad L = nL_s,$$

we get

$$L \frac{di_d}{dt} = -R i_d + \omega L i_q + V \sin \delta, \quad (7)$$

$$L \frac{di_q}{dt} = -\omega L i_d - R i_q - mi_f \omega + V \cos \delta. \quad (8)$$

The angular frequency evolves according to the *swing equation*

$$J \frac{d\omega}{dt} = T_m - T_e - D_p \omega + D_p \omega_n, \quad (9)$$

where $J > 0$ represents the virtual inertia of the rotor, $T_m > 0$ is the nominal active mechanical torque from the prime mover,

$$T_e = -mi_f i_q \quad (10)$$

is the electric torque computed using the measured output currents, ω_n is the nominal grid frequency and $D_p > 0$ is the *frequency droop constant*. We refer to (44) for a way to choose the value of T_m .

We assume here that the inverter works in the linear region of the frequency droop. The actual droop function contains dead-band and saturation, but taking these into account would make the analysis very complicated.

The following equation comes from the definition of δ :

$$\frac{d\delta}{dt} = \omega - \omega_g. \quad (11)$$

The fourth order grid-connected synchronverter model, which considers i_f as a given parameter, can be constructed by combining the equations (7)-(11). Its state vector is

$$\mathbf{x} = [i_d \ i_q \ \omega \ \delta]^T \in \mathbb{R}^4. \quad (12)$$

We write it as a nonlinear dynamical system:

$$\mathbf{H}\dot{\mathbf{x}} = \mathbf{A}(\mathbf{x}, i_f)\mathbf{x} + f(\mathbf{x}), \quad (13)$$

where

$$\mathbf{H} = \begin{bmatrix} L & 0 & 0 & 0 \\ 0 & L & 0 & 0 \\ 0 & 0 & J & 0 \\ 0 & 0 & 0 & 1 \end{bmatrix}, \quad f(\mathbf{x}) = \begin{bmatrix} V \sin \delta \\ V \cos \delta \\ T_m + D_p \omega_n \\ -\omega_g \end{bmatrix},$$

and

$$\mathbf{A}(\mathbf{x}, i_f) = \begin{bmatrix} -R & \omega L & 0 & 0 \\ -\omega L & -R & -mi_f & 0 \\ 0 & mi_f & -D_p & 0 \\ 0 & 0 & 1 & 0 \end{bmatrix}.$$

We now derive the fifth order basic model of a synchronverter, by including i_f into the vector of the state variables. The instantaneous inverter output reactive power is

$$Q = v_q i_d - v_d i_q = V [i_q \sin \delta - i_d \cos \delta], \quad (14)$$

see [20, eq.(16)]. For convenience, we introduce

$$\tilde{Q} = Q_{\text{set}} + D_q \left(v_{\text{set}} - \sqrt{\frac{2}{3}} V \right), \quad (15)$$

where v_{set} is the desired amplitude of v , $D_q > 0$ is the *voltage droop coefficient*, Q_{set} is the desired reactive power, and V is as in (1). Then, the field current i_f evolves according to

$$M_f \frac{di_f}{dt} = \frac{\tilde{Q} - Q}{K}, \quad (16)$$

see [21, eq.(15)], where $K > 0$ is a large constant. We want to make sure that i_f stays in a reasonable operating range $[u_{\min}, u_{\max}]$. (We will say more about this range in Sect. V.) For this, we replace the integrator from (16) with a *saturating integrator* (see [15]), obtaining [21, eq.(21)]:

$$\frac{di_f}{dt} = \mathcal{S} \left(i_f, \frac{\tilde{Q} - Q}{\tilde{K}} \right), \quad (17)$$

where $\tilde{K} = KM_f$. Denoting $w = \frac{\tilde{Q} - Q}{\tilde{K}}$, the function \mathcal{S} is defined by

$$\mathcal{S}(i_f, w) = \begin{cases} w^+ & \text{if } i_f \leq u_{\min}, \\ w & \text{if } i_f \in (u_{\min}, u_{\max}), \\ w^- & \text{if } i_f \geq u_{\max}, \end{cases}$$

where $w^+ = \max\{w, 0\}$, $w^- = \min\{w, 0\}$, so that $w = w^+ + w^-$. This means that as long as i_f is in the range (u_{\min}, u_{\max}) , we have $\frac{di_f}{dt} = \frac{\tilde{Q} - Q}{\tilde{K}}$. However, if i_f reaches one of the end points of $[u_{\min}, u_{\max}]$, it is not allowed to continue out of this interval. (Note that in (17) we use \tilde{K} in place of K because, differently from [21], here i_f is the state, not $M_f i_f$.) Using a saturating integrator in place of a usual one is needed in practice, and also in our stability proof in Sect. V.

The fifth order grid-connected synchronverter model can be constructed by combining (13), (14), and (17) as:

$$\mathbf{H}\dot{\mathbf{x}} = \mathbf{A}(\mathbf{z})\mathbf{x} + f(\mathbf{x}), \quad \frac{di_f}{dt} = \mathcal{S} \left(i_f, \frac{\tilde{Q} - Q}{\tilde{K}} \right), \quad (18)$$

with \mathbf{x} from (12), and with the state $\mathbf{z} = [i_f^x] \in \mathbb{R}^5$. Clearly, we mean that $\mathbf{A}(\mathbf{z}) = \mathbf{A}(\mathbf{x}, i_f)$. If we ignore the saturating feature of \mathcal{S} in (17), and we use (16) (with Q from (14)) instead of (17) for the evolution of i_f (this is true for $i_f \in (u_{\min}, u_{\max})$), i.e.,

$$m \frac{di_f}{dt} = ki_d \cos \delta - ki_q \sin \delta + \frac{k}{V} \tilde{Q}, \quad (19)$$

then we get the fifth order non-saturated model

$$\tilde{\mathbf{H}}\dot{\mathbf{z}} = \tilde{\mathbf{A}}(\mathbf{z})\mathbf{z} + \tilde{f}(\mathbf{z}), \quad (20)$$

where

$$\tilde{\mathbf{H}} = \left[\begin{array}{c|c} \mathbf{H} & \mathbf{0} \\ \hline \mathbf{0} & m \end{array} \right], \quad \tilde{f}(\mathbf{z}) = \left[\begin{array}{c} f(\mathbf{x}) \\ \frac{k}{V} \tilde{Q} \end{array} \right], \quad k = \sqrt{\frac{3}{2}} \frac{V}{K},$$

$$\tilde{\mathbf{A}}(\mathbf{z}) = \left[\begin{array}{ccc|cc} \mathbf{A}(\mathbf{z}) & & & & \mathbf{0} \\ \hline k \cos \delta & -k \sin \delta & 0 & 0 & 0 \end{array} \right],$$

with \mathbf{H} , \mathbf{A} , and f as defined after (13).

An extension of the model (20), to include the effect of measurement errors, has been derived in [11]. This is needed

to analyze the sensitivity of the currents i_d, i_q with respect to the measurement errors. The paper [11] also presents the linearization of the model (20), a typical application example with relevant Bode plots, and experimental results.

The instantaneous active power P to the grid is

$$P = v_d i_d + v_q i_q = -V[i_d \sin \delta + i_q \cos \delta] \quad (21)$$

(see also [21, eq.(17)]), but this is not computed in the control algorithm, except possibly for monitoring. It is easy to derive from (14) and (21) that

$$P^2 + Q^2 = V^2(i_d^2 + i_q^2). \quad (22)$$

We derive a nice formula linking the dq currents and the powers P and Q . We know from (14) and (21) that

$$\begin{bmatrix} P \\ Q \end{bmatrix} = -V \begin{bmatrix} \cos \delta & \sin \delta \\ -\sin \delta & \cos \delta \end{bmatrix} \begin{bmatrix} i_q \\ i_d \end{bmatrix}. \quad (23)$$

By inverting the matrix, we obtain

$$\begin{bmatrix} i_q \\ i_d \end{bmatrix} = -\frac{1}{V} \begin{bmatrix} \cos \delta & -\sin \delta \\ \sin \delta & \cos \delta \end{bmatrix} \begin{bmatrix} P \\ Q \end{bmatrix}. \quad (24)$$

In Sect. III we will study the equilibrium points of the fourth order model (13), and in Sect. IV we will extend the study to the fifth order non-saturated model (20). Finally, the model (18) will be used in Sect. V to derive local exponential stability results for the grid-connected synchronverter.

III. EQUILIBRIUM POINTS OF THE 4TH ORDER GRID-CONNECTED SYNCHRONVERTER

In this section we study the equilibrium points of the fourth order model (13) for the grid-connected synchronverter. Thus, i_f is treated as a parameter here (i.e., there is no field current controller for the reactive power Q). Our main result is a geometric representation of the equilibrium points of (13) in the power plane: We find that, for “reasonable” values of i_f , the images of the corresponding equilibrium points of (13) through the mappings P and Q from (23) move on a circle in the power plane. The radius and centre of this circle depend on the synchronverter parameters, on the grid voltage, and on the prime mover torque at the equilibrium. In addition, the point (P, Q) determines the power angle δ at the equilibrium. Finally, we establish a crucial result for the stability analysis of Sect. V: We find the interval of those field currents $i_f > 0$ for which the reactive power Q corresponding to the relevant equilibrium point is increasing (as a function of i_f).

The equilibrium points of (13) have been explicitly computed in [20, Sect. 3], under the assumption of a constant field current i_f in a reasonable range $I_f \subset (0, \infty)$. For the reader's convenience, we report those results here. In this paper, angles are regarded modulo 2π , i.e., δ and $\delta + 2\pi$ are considered to be the same angle, except for certain arguments in Sect. V.

Assumption 1: Let $R, L, J, m, D_p, V, \omega_g, \omega_n > 0$ and $T_m \in \mathbb{R}$ be given. Denote

$$\tilde{T}_m = T_m + D_p(\omega_n - \omega_g). \quad (25)$$

Assume that

$$4R\omega_g\tilde{T}_m \geq -V^2. \quad (26)$$

Proposition 3.1: Consider the model (13), with \mathbf{x} from (12), and with parameters satisfying Assumption 1. Denote

$$\phi \in \left(0, \frac{\pi}{2}\right) \quad \text{such that} \quad \tan \phi = \frac{\omega_g L}{R}, \quad (27)$$

$$\Lambda(i_f) = -\frac{\tilde{T}_m}{mi_f} \frac{L\sqrt{p^2 + \omega_g^2}}{V} + \frac{mi_f\omega_g p}{V\sqrt{p^2 + \omega_g^2}}, \quad (28)$$

where $p = R/L$. We define the interval $I_f \subset (0, \infty)$ as follows:

$$I_f = \{i_f > 0 \mid |\Lambda(i_f)| \leq 1\}.$$

For any $i_f \in I_f \cup (-I_f)$, the model (13) has two equilibrium points, \mathbf{x}_1^e and \mathbf{x}_2^e , with the power angles δ_1^e and δ_2^e satisfying:

$$\delta_1^e = \arccos \Lambda - \phi, \quad \delta_2^e = -\arccos \Lambda - \phi, \quad (29)$$

where $\arccos \Lambda : [-1, 1] \rightarrow [0, \pi]$. The other components of the equilibrium states \mathbf{x}_j^e are given (for $j \in \{1, 2\}$) by

$$i_{dj}^e = -\frac{\tilde{T}_m\omega_g}{mi_f p} + \frac{V \sin \delta_j^e}{R}, \quad i_q^e = -\frac{\tilde{T}_m}{mi_f}, \quad \omega^e = \omega_g. \quad (30)$$

Note that if $|\Lambda| = 1$, then $\delta_1^e = \delta_2^e$ and thus $\mathbf{x}_1^e = \mathbf{x}_2^e$.

Note that Assumption 1 guarantees that I_f is nonempty.

It is clear from (9) that \tilde{T}_m represents the prime mover torque at equilibrium. The proof follows from [20, Sect. 3], where the notation is slightly different: what is denoted in [20] by T_m , R_s and L_s , is denoted here by $T_m + D_p\omega_n$, R and L , respectively. Moreover, in [20] it is assumed that $i_f > 0$, however the derivations in [20, Sect. 3] remains valid also for $i_f \in (-I_f)$. We now prove that if $\tilde{T}_m \neq 0$, then I_f is a closed interval. If $\tilde{T}_m > 0$, then Λ is an increasing function of i_f , and our claim follows. If, instead, $\tilde{T}_m < 0$, then Λ is first decreasing for a certain interval of i_f , after which it becomes increasing, and we have $\Lambda > 0$ for all $i_f > 0$. Thus, we can conclude again that I_f is a closed interval. Finally, if $\tilde{T}_m = 0$, then Λ depends linearly on i_f and it is clear that I_f is an interval (not closed). The above scenarios are depicted in Fig. 4.

Remark 3.2: As mentioned above, if $\tilde{T}_m > 0$ then Λ is an increasing function of $i_f > 0$ and

$$\{\Lambda(i_f) \mid i_f \in I_f\} = [-1, 1].$$

Thus, for every $\Lambda \in [-1, 1]$, (28) has two solutions:

$$i_{f1} = \frac{\sqrt{p^2 + \omega_g^2} \left(\Lambda V + \sqrt{\Lambda^2 V^2 + 4\omega_g R \tilde{T}_m} \right)}{2m\omega_g p}, \quad (31)$$

and i_{f2} is as above, with $-$ instead of $+$ in front of the square root in the brackets. Clearly $i_{f2} < 0 < i_{f1}$. Thus, there is only one positive solution of (28) for each fixed $\Lambda \in [-1, 1]$.

On the contrary, if $\tilde{T}_m < 0$ then Λ is first a decreasing function of $i_f > 0$, and then an increasing one. Moreover, $\Lambda(i_f) > 0$ for all $i_f > 0$ (see Fig. 4). This implies that

$$\{\Lambda(i_f) \mid i_f \in I_f\} \subset (0, 1],$$

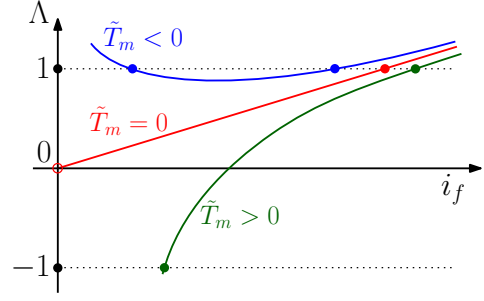


Fig. 4. The plot of $\Lambda(i_f)$ for different values of \tilde{T}_m and for $i_f > 0$.

and that if Λ belongs to the above set, then i_{f1}, i_{f2} from (31) are both positive. Finally, for the case $\tilde{T}_m = 0$, $i_{f2} = 0$ and Λ is linear in i_f , so that $\{\Lambda(i_f) \mid i_f \in I_f\} = (0, 1]$.

Proposition 3.3: We use the notation of Proposition 3.1. Under Assumption 1, if for some $i_f \in I_f$ the model (13) has a stable equilibrium point \mathbf{x}_{st}^e , then $\mathbf{x}_{st}^e = \mathbf{x}_1^e$ and

$$\delta_1^e \in (-\phi, \pi - \phi).$$

Note that if R tends to zero then ϕ tends to $\pi/2$, see (27), and the above condition becomes the famous necessary stability condition $\delta \in (-\frac{\pi}{2}, \frac{\pi}{2})$ appearing often in the literature.

Proof. Denote by $h(\mathbf{x})$ the right-hand side of (13). Let A_{1j} , $j \in \{1, 2\}$, be the Jacobian $A_{1j} = \partial h / \partial \mathbf{x}$ computed at \mathbf{x}_j^e . A necessary condition for the equilibrium point \mathbf{x}_j^e to be stable is that $\mathbf{H}^{-1}A_{1j}$ is a stable matrix, which implies that $\det(\mathbf{H}^{-1}A_{1j}) > 0$. It can be verified easily that

$$\det(\mathbf{H}^{-1}A_{1j}) > 0 \iff \sin(\delta_j^e + \phi) > 0, \quad (32)$$

see [20, eq.(3.5)] for the detailed derivation.

Recall the expressions of δ_1^e and δ_2^e from (29). We have

$$\delta_1^e + \phi \in [0, \pi], \quad \delta_2^e + \phi \in [-\pi, 0].$$

Clearly, (32) holds only for $j = 1$. Thus, $\mathbf{x}_{st}^e = \mathbf{x}_1^e$ and, moreover, we must have $\delta_1^e + \phi \in (0, \pi)$. ■

Proposition 3.4: We use the notation of Proposition 3.1. Consider the model (13), with parameters satisfying Assumption 1, and let $i_f \in I_f \cup (-I_f)$, so that (13) has two equilibrium points. Then, at every equilibrium point of this system we have

$$\tilde{T}_m\omega_g = P + R \frac{P^2 + Q^2}{V^2}. \quad (33)$$

Moreover, the power angle value δ^e at the equilibrium satisfies

$$\tan \delta^e = \frac{\omega_g LP - RQ}{RP + \omega_g LQ + V^2}. \quad (34)$$

Proof. In this proof, for convenience, we omit the superscript e to indicate the equilibrium point values. At an equilibrium point of (13) the left-hand sides of (7) and (8) are zero. We multiply these equations with i_d and i_q , respectively, and we add them using (4), obtaining

$$-R(i_d^2 + i_q^2) - mi_f i_q \omega - v_d i_d - v_q i_q = 0.$$

Using the formulas (10) and (21), we get

$$R(i_d^2 + i_q^2) - T_e \omega + P = 0.$$

It follows from (9) that $T_e = \tilde{T}_m$, and we know from (30) that $\omega = \omega_g$. Substituting these values above, we get

$$\tilde{T}_m \omega_g = P + R(i_d^2 + i_q^2).$$

Using (22) this becomes (33).

Now we turn our attention to (34). If we multiply both sides of (7) (at equilibrium) with $\sin \delta$, both sides of (8) (at equilibrium) with $\cos \delta$ and then we add them, we get

$$m \omega_g i_f \cos \delta = -R[i_d \sin \delta + i_q \cos \delta] + \omega_g L \frac{Q}{V} + V.$$

In the same way, if we multiply (7) with $\cos \delta$, (8) with $\sin \delta$ and we subtract them, we get

$$-m \omega_g i_f \sin \delta = \omega_g L [i_d \sin \delta + i_q \cos \delta] + R \frac{Q}{V}.$$

According to (21) the last two equations can be rewritten as

$$m i_f \omega_g \cos \delta = R \frac{P}{V} + \omega_g L \frac{Q}{V} + V, \quad (35)$$

$$m i_f \omega_g \sin \delta = \omega_g L \frac{P}{V} - R \frac{Q}{V}. \quad (36)$$

Since $i_f \neq 0$, the left sides of (35) and (36) cannot be both zero. We divide the sides of (36) by the sides of (35), which shows that (34) holds. ■

Remark 3.5: The equation (33) has a clear intuitive interpretation: the left-hand side is the mechanical power coming from the virtual prime mover (the frequency droop mechanism is part of the prime mover). The second term on the right-hand side is the power consumed in the output resistors R in series with each of the three phases, if we think of the model as representing a synchronous machine. (This follows from (22) and the fact that the Park transformation is unitary.)

In the following, we present the novel geometric representation of the (manifold of) equilibrium points of (13) in the PQ plane. For this, we first introduce some useful notation.

Notation. We use the notation of Proposition 3.1. Consider the model (13), with parameters satisfying Assumption 1. We define $i_{f-} = \inf I_f$, and $i_{f+} = \sup I_f$. (Depending on the sign of \tilde{T}_m , $\Lambda(i_{f-})$ and $\Lambda(i_{f+})$ take different values, as discussed in Remark 3.2.) Let $\mathbf{x}_1^e(i_f)$, $\mathbf{x}_2^e(i_f)$ be the two equilibrium points of (13) corresponding to $i_f \in I_f$, as described in (29)-(30). ($\mathbf{x}_1^e(i_f)$, $\mathbf{x}_2^e(i_f)$ coincide at $i_f = i_{f-}$ and at $i_f = i_{f+}$.) We denote by $\delta_j(i_f)$ the power angle component of $\mathbf{x}_j^e(i_f)$, $j \in \{1, 2\}$, and by $P_j(i_f)$ ($Q_j(i_f)$) the active (reactive) power at the equilibrium point $\mathbf{x}_j^e(i_f)$, for $j \in \{1, 2\}$. If $X, Y, Z \in \mathbb{R}^2$, then $\widehat{X; Y; Z}$ denotes the angle from the vector $X - Y$ to the vector $Z - Y$ (counterclockwise). We do not distinguish between a vector and the pair of real numbers that are its coordinates.

Theorem 3.6: Consider the model (13), with parameters satisfying Assumption 1. Then the points in \mathbb{R}^2 defined by

$$S_j(i_f) = (P_j(i_f), Q_j(i_f)), \quad i_f \in I_f, \quad j \in \{1, 2\}$$

are on the circle with centre C and radius r given by

$$C = \left(-\frac{V^2}{2R}, 0 \right), \quad r^2 = \frac{V^4 + 4V^2 R \tilde{T}_m \omega_g}{4R^2}. \quad (37)$$

Define the points $Z, M, O \in \mathbb{R}^2$ as

$$Z = (R, \omega_g L), \quad M = -\frac{V^2}{\|Z\|^2} Z, \quad O = (0, 0).$$

Then the distances CO, CM are equal and

$$\widehat{O; M; C} = \widehat{C; O; M} = \phi. \quad (38)$$

Moreover, the following holds:

$$S_j(i_f) - M = \frac{V}{\|Z\|} \begin{bmatrix} \cos(\phi - \delta_j(i_f)) \\ \sin(\phi - \delta_j(i_f)) \end{bmatrix} m i_f \omega_g. \quad (39)$$

Proof. According to Proposition 3.4, the powers $P_j(i_f)$ and $Q_j(i_f)$ satisfy the quadratic equation

$$P_j^2 + Q_j^2 + \frac{V^2}{R} P_j = \frac{\tilde{T}_m \omega_g V^2}{R}.$$

The solutions of this equation are on a circle symmetric with respect to the P axis. The formulas for the centre C and the radius r follow from standard computations.

From a routine computation we get that

$$\|M - C\| = \frac{V^2}{2R} = \|C\|.$$

One conclusion from the above is that the triangle COM is isosceles, and since the angle of Z (with respect to the P axis) is ϕ , we get that (38) holds (see Fig. 5(a), 5(b)).

We now prove (39). For convenience we denote $(P, Q) = (P_j(i_f), Q_j(i_f))$, $\delta = \delta_j(i_f)$. From (7), (8) and (24), we have

$$\frac{1}{V} \begin{bmatrix} R & -\omega L \\ \omega L & R \end{bmatrix} \begin{bmatrix} \cos \delta & \sin \delta \\ -\sin \delta & \cos \delta \end{bmatrix} \begin{bmatrix} Q \\ P \end{bmatrix} + V \begin{bmatrix} \sin \delta \\ \cos \delta \end{bmatrix} = \begin{bmatrix} 0 \\ m i_f \omega_g \end{bmatrix}.$$

Using the definition of ϕ from (27), we have

$$\frac{1}{V} \begin{bmatrix} R & -\omega L \\ \omega L & R \end{bmatrix} = \frac{\|Z\|}{V} \begin{bmatrix} \cos \phi & -\sin \phi \\ \sin \phi & \cos \phi \end{bmatrix}.$$

Substituting this above, commuting the first two matrices, and multiplying with the inverse of the matrix from (23), we obtain

$$\frac{\|Z\|}{V} \begin{bmatrix} \cos \phi & -\sin \phi \\ \sin \phi & \cos \phi \end{bmatrix} \begin{bmatrix} Q \\ P \end{bmatrix} + V \begin{bmatrix} 0 \\ 1 \end{bmatrix} = \begin{bmatrix} -\sin \delta \\ \cos \delta \end{bmatrix} m i_f \omega_g.$$

Multiplying with the inverse of the first matrix above, and also with $V/\|Z\|$, and swapping the rows, we get

$$\begin{bmatrix} P \\ Q \end{bmatrix} + \frac{V^2}{\|Z\|} \begin{bmatrix} \cos \phi \\ \sin \phi \end{bmatrix} = \frac{V}{\|Z\|} \begin{bmatrix} \cos(\phi - \delta) \\ \sin(\phi - \delta) \end{bmatrix} m i_f \omega_g.$$

From here, we get (39) by substituting

$$M = -\frac{V^2}{\|Z\|} \begin{bmatrix} \cos \phi \\ \sin \phi \end{bmatrix}. \quad \blacksquare$$

Remark 3.7: From (39) several useful facts follow. First, taking the norms, we have that (for $i_f \in I_f$)

$$\|S_j(i_f) - M\| = \frac{V}{\|Z\|} m i_f \omega_g, \quad (40)$$

i.e., the distance from $S_j(i_f)$ to M is proportional to i_f . This implies that the level curves in the power plane for constant i_f are circles, with centre M and radius given by (40). Second,

(39) tells us that the vector $S_1(i_f) - M$ forms an angle of $\phi - \delta_1$ with the P axis (see Fig. 5(a), 5(b)). Thus,

$$\widehat{S_1(i_f); M; O} = \phi - (\phi - \delta_1) = \delta_1.$$

Third, clearly $i_{f-} \leq i_f \leq i_{f+}$, for any $i_f \in I_f$. From (40), $S_1(i_{f-})$ is the point on the circle from Theorem 3.6 that is the closest to M , while $S_1(i_{f+})$ is the point on the same circle that is the farthest from M . This implies that $S_1(i_{f-}), M, C$ and $S_1(i_{f+})$ are on a straight line \mathcal{L} , as in Fig. 5(a), 5(b).

From the above facts it follows that, for increasing $i_f \in I_f$, the point $S_1(i_f)$ moves counterclockwise on the circle described in Theorem 3.6, from $S_1(i_{f-})$ to $S_1(i_{f+})$.

Remark 3.8: It follows from the formula for r in (37) that, depending on the sign of \tilde{T}_m , three scenarios are possible for the points M and O from Theorem 3.6: If $\tilde{T}_m > 0$ then M, O are inside the circle, while if $\tilde{T}_m < 0$ ($\tilde{T}_m = 0$) then M, O are outside (on) the circle. The case $\tilde{T}_m > 0$ is the most common.

Theorem 3.9: We use the notation of Theorem 3.6. Let Assumption 1 hold. Then:

(a) If $\omega_g L > R$, then M is to the right of C . There is a unique $i_{f0} \in I_f$ for which $S_1(i_{f0}) = (-V^2/2R, r)$ and

$$\frac{d}{di_f} Q_1(i_f) > 0 \quad \text{for } i_f \in I_f^+ = (i_{f-}, i_{f0}).$$

(b) If $\omega_g L \leq R$, then M is to the left of (or directly below) C . There is a unique $i_{f0} \in I_f$ for which $S_1(i_{f0}) = (-V^2/2R, -r)$ and

$$\frac{d}{di_f} Q_1(i_f) > 0 \quad \text{for } i_f \in I_f^+ = (i_{f0}, i_{f+}).$$

Theorems 3.6, 3.9 are illustrated in Fig. 5(a), 5(b). As discussed in Remark 3.7, we see that $S_1(i_f)$ moves counterclockwise on the circle, for increasing i_f , from $S_1(i_{f-})$ to $S_1(i_{f+})$, while $S_2(i_f)$ moves clockwise between the same two endpoints. The movement of $S_2(i_f)$ is symmetric to the one of $S_1(i_f)$, with respect to the line \mathcal{L} .

Note that the case $\omega_g L > R$ is the most common.

Proof of Theorem 3.9. Let $\tilde{T}_m \geq 0$. In the case (a), an elementary computation shows that the P -coordinate of M is larger than that of C :

$$-\frac{V^2 R}{\|Z\|^2} > -\frac{V^2}{2R}.$$

Hence, M is to the right of C , as stated. Note that this implies that the slope of \mathcal{L} is negative, as in Fig. 5(a).

As discussed in Remark 3.7, $S_1(i_f)$ moves counterclockwise on the circle for increasing $i_f \in I_f$. Since i_f is proportional to the distance from S_1 to M , Q_1 is strictly increasing (with positive derivative) for $i_f \in I_f^+ = (i_{f-}, i_{f0})$, where i_{f0} is the field current for which $Q_1(i_f)$ reaches its maximum value, namely r . From Fig. 5(a) we see that i_{f0} is the unique field current for which $P_1(i_{f0}) = -V^2/2R$.

We move now to case (b). We perform the same elementary computation as before, reaching the opposite conclusion for $\omega_g L \leq R$, namely, that M is to the left of (or directly below) C . Thus, for $\omega_g L < R$, the slope of \mathcal{L} is positive (as depicted in Fig. 5(b)), and for $\omega_g L = R$, \mathcal{L} is vertical.

In the proof of (b), the interval on which Q_1 is increasing is from i_{f0} , where Q_1 is at its minimum, until i_{f+} . We see from Fig. 5(b) that $S_1(i_{f0}) = (-V^2/2R, -r)$.

The proof of the case $\tilde{T}_m < 0$ is similar. \blacksquare

Remark 3.10: For $\tilde{T}_m < 0$ both the solutions i_{f1}, i_{f2} of (28), with $\Lambda \in \{\Lambda(i_f) \mid i_f \in I_f\}$, are positive (see Remark 3.2). This has an intuitive geometrical meaning. Fixing Λ is similar to fixing $\lambda = \arccos \Lambda$, i.e., the angle $\widehat{S_1(i_{f1}); M; C}$ in Fig. 6. Since M is outside of the circle (see Remark 3.8), the line passing through the points M and $S_1(i_{f1})$ cuts the circle in another point, namely, $S_1(i_{f2})$. The values i_{f1}, i_{f2} are the two (positive) solutions of (28) mentioned above. The case $S_1 \equiv S_1'$ in Fig. 6 corresponds to the value of Λ for which the square root in (31) is zero, i.e., $i_{f1} = i_{f2}$.

Remark 3.11: The point $S_1(i_f)$ moves counterclockwise on the circle described in Theorem 3.6, from $S_1(i_{f-})$ to $S_1(i_{f+})$ for increasing $i_f \in I_f$, as discussed in Remark 3.7. When $\tilde{T}_m \geq 0$, this implies that $\delta_1(i_f)$ is decreasing from $\delta_1(i_{f-}) = \pi - \phi$, to $\delta_1(i_{f+}) = -\phi$. However, when $\tilde{T}_m < 0$ then this is not true. Indeed $\delta_1(i_{f-}) = \delta_1(i_{f+}) = -\phi$.

IV. EQUILIBRIUM POINTS OF THE FIFTH ORDER GRID-CONNECTED SYNCHRONVERTER

In this section we study the equilibrium points of the fifth order grid-connected synchronverter model (20). Using the results for the fourth order model (13) from the previous section, we derive a necessary and sufficient condition for the existence of the equilibrium points of (20) (where i_f is a state variable) and we compute them explicitly. As in Sect. III, we consider the grid to be an infinite bus, with constant V, ω_g .

The fifth order model (18) or (20) is shown as a block diagram in Fig. 7, with the fourth order model (13) as a block.

Assumption 2: Let $R, L, J, m, D_p, D_q, V, \omega_g, \omega_n, v_{\text{set}} > 0$ and $T_m, Q_{\text{set}} \in \mathbb{R}$ be given.

Our first result concerns mainly the equation that must be satisfied by the active power P at an equilibrium point of (20).

Proposition 4.1: Consider the model (20), with parameters satisfying Assumption 2. Recall \tilde{Q} from (15) and \tilde{T}_m from (25).

A necessary condition for this system to have equilibrium points is

$$4R^2 \tilde{Q}^2 \leq V^4 + 4RV^2 \tilde{T}_m \omega_g. \quad (41)$$

At every equilibrium point of this system we have

$$\omega = \omega_g, \quad T_e = \tilde{T}_m, \quad Q = \tilde{Q}, \quad (42)$$

and P satisfies the equation

$$\tilde{T}_m \omega_g = P + R \frac{P^2 + \tilde{Q}^2}{V^2}. \quad (43)$$

Remark 4.2: A formula equivalent to (43) has appeared in [21, eq.(24)], but instead of a mathematical proof it was derived from a physical balance equation. As proposed in [21], this formula can be used in the synchronverter algorithm to determine the value of the parameter T_m , if the reference values P_{set} and Q_{set} are given and if some estimate (for instance, zero) is adopted for the differences $\omega_n - \omega_g$ and $v_{\text{set}} - \sqrt{2}/3V$.

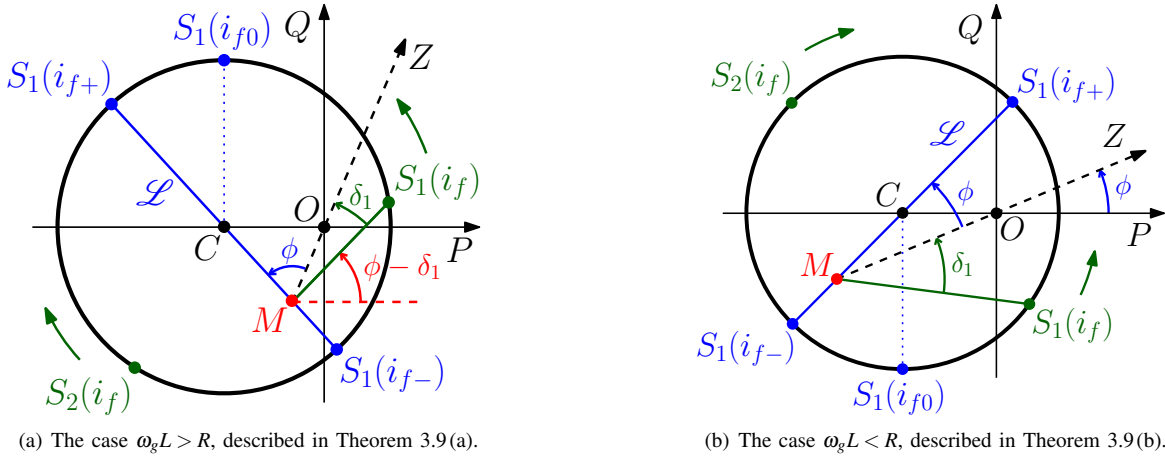


Fig. 5. The circles (for $\tilde{T}_m > 0$) on which the vectors $S_1(i_f)$ and $S_2(i_f)$ move. The green arrows indicate the movement of $S_1(i_f)$ and $S_2(i_f)$ for increasing i_f .

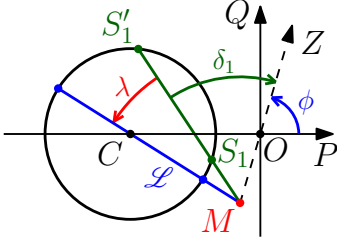


Fig. 6. The circle corresponding to $\tilde{T}_m < 0$ and $\omega_g L > R$. We have denoted $S_1' = S_1(i_{f1})$ and $S_1 = S_1(i_{f2})$ ($0 < i_{f2} \leq i_{f1}$). The case $\omega_g L \leq R$ is similar, but derived according to Fig. 5(b).

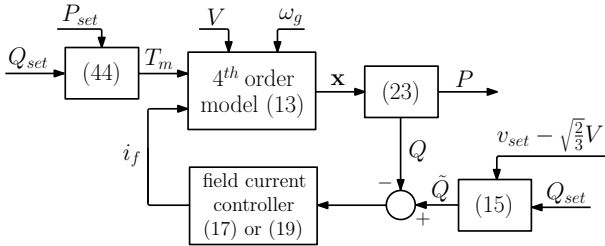


Fig. 7. The fourth order model (13) as a subsystem of the fifth order models (18), (20). Depending on the usage of (17) or (19) in the field current controller, we get respectively (18) or (20).

Indeed, if the estimate zero is adopted for these differences (which is, a priori, our best guess), then

$$T_m \omega_n = P_{\text{set}} + R \frac{P_{\text{set}}^2 + Q_{\text{set}}^2}{V^2}. \quad (44)$$

For this reason, it is similar to assume that T_m , Q_{set} are given (as in Proposition 4.1) or that P_{set} , Q_{set} are given.

Note that (41) is equivalent to $|\tilde{Q}| \leq r$, where r is the radius of the circle from Proposition 3.6. Indeed, $|\tilde{Q}| > r$ would be an infeasible requirement, as is clear from Fig. 5(a), 5(b).

Proof. We omit the superscript e to indicate the equilibrium point values. If the system is at an equilibrium point, then from (11) we see immediately that $\omega = \omega_g$, from (9) we see that $T_e = \tilde{T}_m$ and from (16) we see that $Q = \tilde{Q}$. Thus, we have proved all the parts of (42).

Equation (43) follows from (33), substituting $Q = \tilde{Q}$ from (42). Note that (43) is a second order equation in P , where

the coefficients depend on the parameters of the system. For this equation to have a real solution, by elementary algebra, the condition (41) must be satisfied. Hence, if (41) does not hold, then the system cannot have equilibrium points. ■

Remark 4.3: The equilibrium points of (20) come in symmetric pairs. Indeed, if $\mathbf{z}^e = [i_d^e \ i_q^e \ \omega_g \ \delta^e \ i_f^e]^\top$ is such an equilibrium point, then also

$$\tilde{\mathbf{z}}^e = [-i_d^e \ -i_q^e \ \omega_g \ \delta^e + \pi \ -i_f^e]^\top$$

is an equilibrium point. The intuition behind this is clear: if we rotate the rotor by 180° and at the same time invert the current i_f in the rotor, then by the symmetry of the rotor nothing has really changed. The replacement of the rotor angle θ with $\theta + \pi$ causes i_d and i_q to change sign, while the currents in the stationary frame remain unchanged. We see from (23) that the active and reactive powers P, Q at \mathbf{z}^e and at $\tilde{\mathbf{z}}^e$ are the same.

Remark 4.4: The system (20) has an exceptional set of equilibrium points corresponding to the point M defined in Theorem 3.6. Indeed, when the circle defined in Theorem 3.6 passes through the point M (this happens for $\tilde{T}_m = 0$), and the values of P and \tilde{Q} are the coordinates of M , namely

$$P = -\frac{V^2 R}{R^2 + \omega_g^2 L^2}, \quad \tilde{Q} = -\frac{V^2 \omega_g L}{R^2 + \omega_g^2 L^2}, \quad (45)$$

then if we choose $i_f^e = 0$ and any angle δ^e , we get an equilibrium point of (20). This can be checked through a somewhat tedious computation (using (24)), which shows that for $i_f^e = 0$ and any δ^e , (7) and (8) hold with zero on the left-hand side. The other equilibrium equations are easily seen to hold. Thus, for $\tilde{T}_m = 0$ and P, \tilde{Q} as in (45) we have infinitely many equilibrium points.

The physical interpretation of these equilibrium points is as follows: here the rotor has no current and hence no magnetic field, so that its angle is irrelevant for what happens in the stator windings. The SG now consists of only the stator windings connected to the power grid, consuming power. The practical importance of the exceptional set of equilibrium points discussed above is very small, along with all the equilibrium points that correspond to negative i_f . Indeed, the

actual field current controller employs a saturating integrator (see (17)), which constrains the i_f values to an interval of positive numbers (contained in I_f). This is a safety feature that prevents the system from leaving its normal operating range.

Theorem 4.5: We work with the notation of Proposition 4.1. Then the model (20), with parameters satisfying Assumption 2, has equilibrium points if and only if (41) is satisfied. Suppose that the condition (41) is true, and let us denote by P_l and P_r the two real solutions of (43), so that $P_l \leq P_r$, and $\frac{P_l + P_r}{2} = -\frac{V^2}{2R}$. At every equilibrium point we have $P = P_l$ or $P = P_r$.

Recall the exceptional point M discussed in the last remark. Assume that the equilibrium point is such that $(P, \tilde{Q}) \neq M$. Then the angle δ^e satisfies

$$\tan \delta^e = \frac{\omega_g L P - R \tilde{Q}}{R P + \omega_g L \tilde{Q} + V^2}. \quad (46)$$

If the angle δ is measured modulo 2π , and (41) holds with strict inequality, then the model (20) has precisely four equilibrium points. Two of them, denoted by \mathbf{z}_r^e and \mathbf{z}_l^e , have the property that $i_f^e > 0$. At \mathbf{z}_r^e , $P = P_r$, and at \mathbf{z}_l^e , $P = P_l$. There are also the two symmetric equilibrium points $\tilde{\mathbf{z}}_r^e$ and $\tilde{\mathbf{z}}_l^e$ where $i_f^e < 0$, as described in Remark 4.3. If (41) holds with equality, then $P_l = P_r = -V^2/2R$ and the model has precisely two equilibrium points, which are a symmetric pair.

Remark 4.6: We see from (46) that to any $(P, \tilde{Q}) \neq M$ in the power plane correspond two possible equilibrium angles, that differ by π . This is true also if the denominator is zero, in that case $\delta^e = \pm\pi/2$. For the exceptional pair M , the right-hand side of (46) is 0/0, so that δ^e could take any value, in accordance with Remark 4.4.

Proof. We omit the superscript e to indicate the equilibrium point values. Assume that (41) holds, so that (43) has two real solutions, P_l and P_r , with $P_l \leq P_r$. We know from Proposition 4.1 that at every equilibrium point, $P = P_l$ or $P = P_r$.

Equation (46) follows from (34), substituting $Q = \tilde{Q}$ from (42). For each choice of P (either P_l or P_r) such that $(P, \tilde{Q}) \neq M$, this equation has precisely two solutions modulo 2π , that differ by an angle of π . (In the extreme case when the denominator in (46) is zero, then the solutions are $\pm\pi/2$.)

Suppose that (41) holds with strict inequality, which implies that $P_l < P_r$, and suppose that $(P, \tilde{Q}) \neq M$. Then we obtain four candidate equilibrium angles δ (two for $P = P_l$ and two for $P = P_r$). We now show that each of these four angles actually corresponds to an equilibrium point $\mathbf{z} = (i_d, i_q, \omega_g, \delta, i_f)$. From (24) we see that at any equilibrium point

$$\begin{bmatrix} i_q \\ i_d \end{bmatrix} = -\frac{1}{V} \begin{bmatrix} \cos \delta & -\sin \delta \\ \sin \delta & \cos \delta \end{bmatrix} \begin{bmatrix} P \\ \tilde{Q} \end{bmatrix},$$

where $P = P_l$ or $P = P_r$. From (10) and (42) we see that at any equilibrium point,

$$\tilde{T}_m = -m i_f i_q.$$

Thus, if $\tilde{T}_m \neq 0$, i_f can be computed from here. If $\tilde{T}_m = 0$, then (8) (at the equilibrium) should be used instead, as long as $(P, \tilde{Q}) \neq M$. The exceptional case when $(P, \tilde{Q}) = M$ leads to $i_f = 0$ and arbitrary δ , as discussed in Remark 4.4.

It is easy to see that the points $\mathbf{z} = (i_d, i_q, \omega_g, \delta, i_f)$ computed as described are indeed equilibrium points, and they come in two symmetric pairs, as described in Remark 4.3.

When we have equality in (41), then $P_l = P_r = -V^2/2R$. Correspondingly, there are only two solutions for (46) (modulo 2π) and they differ by π . The currents i_d, i_q, i_f are computed as before, and we obtain two equilibrium points (a symmetric pair), one with $i_f > 0$ and the other one with $i_f < 0$. ■

Remark 4.7: Under the conditions of the last theorem, it is easy to see that $P_r \geq 0$ if and only if

$$R \tilde{Q}^2 \leq V^2 \tilde{T}_m \omega_g, \quad (47)$$

and $P_r = 0$ if and only if we have equality in (47). Note that (47) implies (41) and we always have $P_l < 0$. If an equilibrium point corresponds to $P_r > 0$ and $\tilde{Q} = 0$, then $\tan \delta^e > 0$ (this means that $\delta^e \in (0, \pi/2) \cup (\pi, 3\pi/2)$). Indeed, this can be seen directly from (46). (These facts are clear from Fig. 5(a), 5(b).)

Remark 4.8: As mentioned at the end of Remark 4.4, the real system (18) can never reach the two equilibrium points with $i_f^e \leq 0$, due to the saturating integrator used in the field current controller (see (17)).

V. STABILITY OF THE GRID-CONNECTED SYNCHRONVERTER

In this section we investigate the stability of the grid-connected synchronverter model (18) using [15, Theorem 4.3], which is based on singular perturbation theory. Our main result in Theorem 5.2 proves that, under reasonable assumptions, there exists a $\kappa > 0$ such that if $\tilde{K} > \frac{1}{\kappa}$, then the fifth order model (18) has a (locally) exponentially stable equilibrium point with a “large” domain of attraction. This stable equilibrium point “corresponds” to \mathbf{x}_1^e from Proposition 3.1. After stating our main result, we offer a visual representation of the stability region of the fifth order model (18), based on the geometric description introduced in Proposition 3.6.

Note that results closely related to our Theorem 5.2, with most of the proof missing, assuming that the model (13) is almost globally asymptotically stable for every constant $i_f \in [u_{min}, u_{max}]$, have been presented in [21, Theorem 5.1].

We introduce a function Ξ that maps “reasonable” values of i_f into the corresponding first equilibrium point \mathbf{x}_1^e of the fourth order model (13) (see Proposition 3.1) as

$$\Xi: I_f \rightarrow \mathbb{R}^4 \quad \text{such that} \quad \Xi(i_f) = [i_{d1}^e \ i_q^e \ \omega_g \ \delta_1^e]^\top, \quad (48)$$

where i_{d1}^e, i_q^e and δ_1^e are given by (29)-(30), so that $\mathbf{x}_1^e = \Xi(i_f)$. Here angles are not identified modulo 2π , because we use results from singular perturbations theory that have been formulated for systems evolving on \mathbb{R}^n . We consider $\delta_1^e \in [-\pi, \pi]$.

Recall the interval I_f^+ from Theorem 3.9. Then it follows from the just mentioned theorems that if (26) holds with strict inequality (so that I_f^+ is nonempty), then

$$\frac{d}{di_f} Q_1(i_f) > 0 \quad \text{for} \quad i_f \in I_f^+.$$

Let $\mathbf{z}_r^e = [i_{dr}^e \ i_{qr}^e \ \omega_g \ \delta_r^e \ i_{fr}^e]^\top$ be defined as in Theorem 4.5 (i.e., \mathbf{z}_r^e is the equilibrium point of the fifth order model (20) at which $i_{fr}^e > 0$ and $P = P_r$). Assume that $i_{fr}^e \in I_f^+$. We see from Fig. 5(a) and Fig. 5(b) that this implies that the point $(P_1(i_{fr}^e), Q_1(i_{fr}^e))$ is to the right of the line \mathcal{L} in the power plane, so that $P_1(i_{fr}^e) = P_r$ and thus

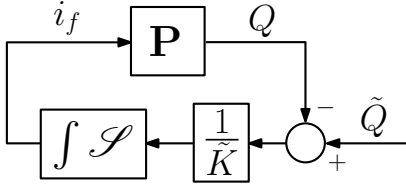


Fig. 8. The closed-loop system (18) formed by the plant \mathbf{P} from (13), \tilde{Q} from (15), and the saturating integrator from (17).

$$\mathbf{z}_r^e = \begin{bmatrix} \Xi(i_{fr}^e) \\ i_{fr}^e \end{bmatrix}.$$

Proposition 5.1: We consider the fourth order system \mathbf{P} described by (13), with parameters satisfying Assumption 1 ((26) with strict inequality). Recall the function Ξ from (48). Let $u_{min} < u_{max}$ in \mathbb{R} and $\varepsilon > 0$ be such that $U_\varepsilon = [u_{min} - \varepsilon, u_{max} + \varepsilon] \subset I_f^+$. Denote by $G: U_\varepsilon \rightarrow \mathbb{R}$ the steady-state input-output map associated to \mathbf{P} , with input i_f and output $Q_1(i_f)$, i.e., $G(i_f)$ is the output $Q_1(i_f)$ at $\mathbf{x} = \Xi(i_f) = \mathbf{x}_1^e$. Then,

$$G'(i_f) > 0, \quad \forall i_f \in U_\varepsilon.$$

Proof. It follows from Theorem 3.9 that $Q_1(i_f)$ is increasing for $i_f \in I_f^+$. Thus, $G'(i_f) > 0$ for all $i_f \in U_\varepsilon \subset I_f^+$. ■

Theorem 5.2: Consider the model (18), with given $R, L, J, m, D_p, D_q, V, \omega_g, \omega_n, v_{set} > 0$ and $T_m \in \mathbb{R}$, and with the state $\mathbf{z} = \begin{bmatrix} \mathbf{x} \\ i_f \end{bmatrix} \in \mathbb{R}^5$ (\mathbf{x} is as in (12)). We use the notation $\mathbf{P}, \tilde{T}_m, I_f, I_f^+, u_{min}, u_{max}, \varepsilon, U_\varepsilon, \Xi, G$ as in Proposition 5.1. Assume that (26) holds with strict inequality and that the synchronverter parameters are chosen so that \mathbf{P} has a locally exponentially stable equilibrium point for every $i_f \in U_\varepsilon$.

Then, for any $\tilde{Q} \in [G(u_{min}), G(u_{max})]$, denoting $i_{fr}^e = G^{-1}(\tilde{Q})$, there exist an $\varepsilon_0 > 0$ and a $\kappa > 0$ such that: If $\tilde{K} > \frac{1}{\kappa}$, then $\mathbf{z}_r^e = (\Xi(i_{fr}^e), i_{fr}^e)$ is a (locally) exponentially stable equilibrium point of the closed-loop system (18), with state space $X = \mathbb{R}^4 \times [u_{min}, u_{max}]$. Moreover, if the initial state $(\mathbf{x}(0), i_f(0)) \in X$ of (18) satisfies $\|\mathbf{x}(0) - \Xi(i_f(0))\| \leq \varepsilon_0$, then

$$\mathbf{x}(t) \rightarrow \Xi(i_{fr}^e), \quad i_f(t) \rightarrow i_{fr}^e, \quad Q(t) \rightarrow \tilde{Q},$$

and this convergence is at an exponential rate.

Proof. The exponential stability of \mathbf{P} for each $i_f \in U_\varepsilon$ (as assumed in the theorem) implies the uniform exponential stability of \mathbf{P} , see [15, Remark 3.1]. This, together with the result from Proposition 5.1, allows us to apply [15, Theorem 4.3], completing the proof of the theorem. ■

Remark 5.3: The local exponential stability assumption in the above theorem is true if the parameters satisfy the numerical conditions presented in [3, Theorem 1] or in [20, Theorem 6.3] (the conditions in these two references are not equivalent). Actually, [3] and [20] conclude aGAS.

We now illustrate how to derive the region of stability of the fifth order model (18) in the power plane. We assume that the inverter parameters, as well as V and ω_g , are known and fixed, but P_{set} and Q_{set} can vary. Recall the notation of Theorems 3.9, 4.5. Then the coordinates of $\mathbf{z}_r^e = S_1(i_{fr}^e)$ can be obtained from (P_{set}, Q_{set}) as follows:

- If $\omega_n = \omega_g$ and $v_{set} = \sqrt{\frac{2}{3}}V$, i.e., the grid is in nominal conditions, then $S_1(i_{fr}^e) = (P_{set}, Q_{set})$.
- If the grid is not in nominal conditions, T_m is computed from (44), \tilde{T}_m is given by (25), and \tilde{Q} is computed according to (15). Finally, P is the larger of the two solutions of (43) and $S_1(i_{fr}^e) = (P, \tilde{Q})$.

According to Proposition 4.1, $Q = \tilde{Q}$ at both the equilibrium points \mathbf{z}_r^e and \mathbf{z}_l^e of (18), and they both satisfy (43). Hence, \mathbf{z}_r^e and \mathbf{z}_l^e are located on the circle with radius r and centre C given by (37), as show in Fig. 9.

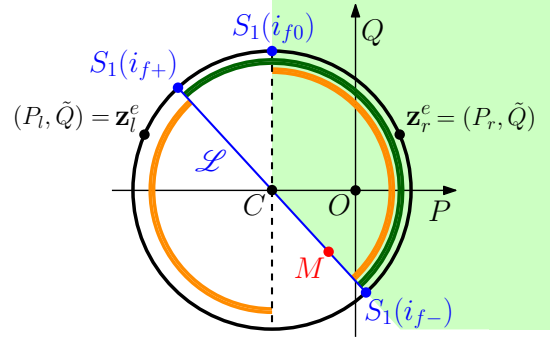


Fig. 9. The circle on which the equilibrium points \mathbf{z}_r^e and \mathbf{z}_l^e of (18) are located for a fixed \tilde{T}_m . (Here we assume that $\omega_g L > R$, so that \mathcal{L} has a negative slope. The case $\omega_g L \leq R$ is similar, but derived according to Fig. 5(b).) The green semicircle is the stability region of (13) on the circle, the orange arcs indicate the region on the circle where $G'(i_f) > 0$, while the light green area denotes the stability region of (18), for varying P_{set}, Q_{set} .

According to our experience (see Examples VI-A, VI-B), for usual synchronverter parameters and normal operating conditions, the equilibrium points $\mathbf{x}_1^e(i_f)$ of the fourth order model (13) are stable for all $i_f \in I_f$. This semicircle is indicated in dark green in Fig. 9. On the other hand, Theorem 5.2 tells us that the equilibrium points \mathbf{z}_r^e of the fifth order model (18) given by $\mathbf{z}_r^e = (\Xi(i_{fr}^e), i_{fr}^e)$, where $i_{fr}^e \in I_f$ is such that $\mathbf{x}_1^e(i_{fr}^e)$ is stable and $G'(i_{fr}^e) > 0$, are stable. Thus, if we indicate in orange the region of the circle where $G'(i_{fr}^e) > 0$ (see Fig. 9), its intersection with the green semicircle gives the region where the assumptions of Theorem 5.2 hold. From here, it follows that, for different values of P_{set} and Q_{set} (i.e. different values of \tilde{T}_m), the stability region of the resulting fifth order model (18) is contained in the green conic sector in Fig. 9. As will be illustrated in Examples VI-A, VI-B, the stability region of (18) in the power plane depends on the value of \tilde{K} . Indeed, from our computations we see that (for fixed synchronverter parameters) the stability region is changing for different values of \tilde{K} . Surprisingly, it seems that, even though the overall stability region area $A(\tilde{K})$ is increasing for increasing values of \tilde{K} , it is not true that if $\tilde{K}_1 > \tilde{K}_2$ then $A(\tilde{K}_2) \subset A(\tilde{K}_1)$. Moreover, Theorem 5.2 states that if (13) is stable and $i_f \in I_f^+$, then also (18) must be stable for sufficiently large values of \tilde{K} . However, the converse is not true. Indeed, it can happen that (18) is stable for some values of \tilde{K} in regions of the power plane where (13) is not, as discussed in the numerical examples of Sect. VI.

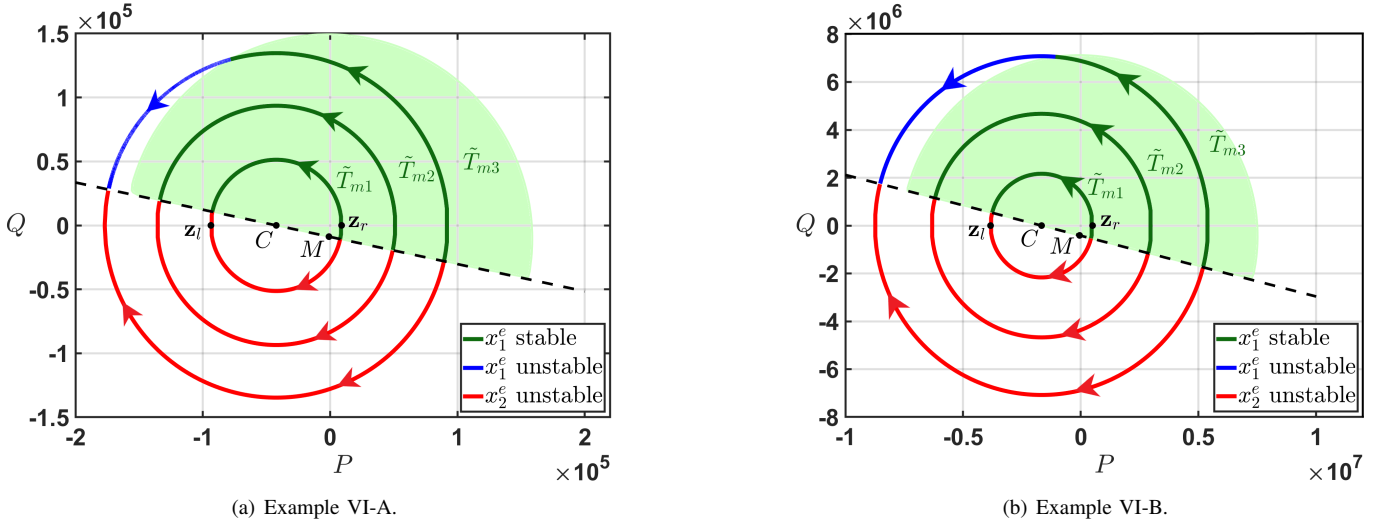


Fig. 10. The circles are representing the equilibrium points of the fourth order model (13) in the power plane, with the parameters from Example VI-A (Subfig. a) and from Example VI-B (Subfig. b), for different values of \tilde{T}_m from (25). The legend refers to the coloured arcs, and \mathbf{x}_1^e , \mathbf{x}_2^e are from Proposition 3.1. The light green area denotes the maximal stability region of (13), with the parameters from Example VI-A (Subfig. a) and from Example VI-B (Subfig. b). The points C, M are from Proposition 3.6, while $\mathbf{z}_l, \mathbf{z}_r$ are from Theorem 4.5.

VI. NUMERICAL EXAMPLES

In this section, we use two examples from the synchronverter literature to illustrate our theoretical derivations: Example VI-A is taken from [12], and Example VI-B from [20]. The focus is the stability analysis of the fourth order model (13), and of the fifth order model (18), for varying values of P_{set} and Q_{set} . We will show how the novel geometrical representation from Fig. 5(a), 5(b) is indeed appearing naturally when studying the stability of the equilibrium points of (13) for $i_f \in I_f$, and we will show how the green conic sector from Fig. 9, corresponding to the stability region of (18), depends on the value of \tilde{K} .

A. Low-voltage synchronverter

We use the parameters of a synchronverter designed to supply a nominal active power of 9kW to a grid with frequency $\omega_g = 100\pi$ rad/sec (50Hz) and line voltage $V = 230\sqrt{3}$ Volts. This is based on a real inverter that we have built, see [12]. The parameters are: $J = 0.2$ Kg·m²/rad, $D_p = 3$ N·m/(rad/sec), $L_s = 2.27$ mH, $R_s = 0.075\Omega$, $K = 5$ kA, $n = 25$, $D_q = 0$ VAR/Volt, $m = 3.5$ H. For simplicity we let $v_{\text{set}} = \sqrt{\frac{2}{3}}V = 325.26$ Volt, $Q_{\text{set}} = 0$ VAR, so that $\tilde{Q} = 0$. We take $T_m = 31.69$ Nm (according to (44), this mechanical torque corresponds to $P_{\text{set}} = 9$ kW and $Q_{\text{set}} = 0$ VAR). We have $R = nR_s = 1.875\Omega$, $L = nL_s = 56.75$ mH, and $\phi = 83.99^\circ$.

From Theorem 4.5 we know that there are four equilibrium points. We are interested in \mathbf{z}_r^e , \mathbf{z}_l^e , i.e., those corresponding to positive i_f values at the equilibrium. These can be computed as explained in Sect. IV, yielding:

$$\mathbf{z}_r^e = \begin{bmatrix} i_{dr}^e \\ i_{qr}^e \\ \omega_g \\ \delta_r \\ i_{fr}^e \end{bmatrix} = \begin{bmatrix} -15.24 \\ -16.68 \\ 314.16 \\ 42.42^\circ \\ 0.54 \end{bmatrix}, \quad \mathbf{z}_l^e = \begin{bmatrix} i_{dl}^e \\ i_{ql}^e \\ \omega_g \\ \delta_l^e \\ i_{fl}^e \end{bmatrix} = \begin{bmatrix} -235.04 \\ -2.38 \\ 314.16 \\ -90.58^\circ \\ 3.81 \end{bmatrix}.$$

We mention that if we compute the active power P at the above two equilibrium points according to (21), we get that

$P_r = 9$ kW at the stable equilibrium point (which is exactly P_{set}), and $P_l = -93.64$ kW at the unstable equilibrium point. This corresponds to what we expected, based on Theorem 4.5.

The equilibrium points \mathbf{z}_r^e corresponding to (P_r, \tilde{Q}) and \mathbf{z}_l^e corresponding to (P_l, \tilde{Q}) are depicted in Fig. 10(a), on the smallest circle, which corresponds to $\tilde{T}_{m1} = 31.69$ N·m, i.e., to $P_{\text{set}} = 9$ kW and $Q_{\text{set}} = 0$ Var. For this circle, we get $I_{f1} = [0.37, 3.83]$ A. In the same figure, we also show two other circles, corresponding to the equilibrium points of (13) for $\tilde{T}_{m2} = 261.64$ N·m (i.e., $P_{\text{set}2} = 50$ kW and $Q_{\text{set}2} = 15$ kVar) and $\tilde{T}_{m3} = 614.60$ N·m (i.e., $P_{\text{set}3} = 90$ kW and $Q_{\text{set}3} = 25$ kVar), for which, respectively, we get $I_{f2} = [2.10, 5.56]$ A and $I_{f3} = [3.78, 7.24]$ A. Note that $\tilde{T}_m = T_m$, since $\omega_g = \omega_n$. As we can see from Fig. 10(a), while the equilibrium points \mathbf{x}_2^e are always unstable, which is a known fact according to Proposition 3.3, the equilibrium points \mathbf{x}_1^e in this example are always stable for reasonable (i.e., not too large) P_{set} and Q_{set} values. This can be checked by computing the eigenvalues of the linearizations.

The light green area in Fig. 10(a) indicates the stability region of the fourth order model (13), which indeed covers all the relevant (P, Q) values. We mention an interesting observation: it seems from our numerical results that the point M coincides with the centre of the green semidisk in Fig. 10(a), indicating the stability region of (13).

In Fig. 11(a) we show how the contour of the fifth order model (18) stability region varies for different values of \tilde{K} . We use the following values: $\tilde{K}_1 = 2.5$ kA·H, $\tilde{K}_2 = 14.3$ kA·H, $\tilde{K}_3 = 40$ kA·H, and $\tilde{K}_4 = 1000$ kA·H. Note that \tilde{K}_2 is the value corresponding to $K = 5$ kA, i.e., the one used above for the computation of \mathbf{z}_l^e and \mathbf{z}_r^e . Even though the overall stability region area $A(\tilde{K})$ is increasing for increasing values of \tilde{K} , it is not true that if $\tilde{K}_1 > \tilde{K}_2$, then $A(\tilde{K}_2) \subset A(\tilde{K}_1)$, as is clear from Fig. 11(a). We mention that, for $\tilde{K} \rightarrow \infty$, it seems from our numerical results that the region of stability of (18) coincides with the intersection of the green sector from Fig. 9 and of the stability region of (13). This can be observed in Fig. 11(a),

where, for increasing values of \tilde{K} , the stability region contours approach the boundary of the light green area.

B. High-voltage synchronverter

We consider a synchronverter from [20] that supplies a nominal active power of 500kW to a grid with frequency $\omega_g = 100\pi$ rad/sec (50Hz) and line voltage $V = 6000\sqrt{3}$ Volts. The parameters are: $J = 20.26$ Kg·m²/rad, $D_p = 168.87$ N·m/(rad/sec), $L_s = 27.5$ mH, $R_s = 1.08$ Ω , $K = 5000$ A, $n = 30$, $D_q = 0$ VAr/Volt, $m = 33$ H. As previously, we let $v_{set} = \sqrt{\frac{2}{3}}V = 8485.3$ Volt, $Q_{set} = 0$ VAr, so that $\tilde{Q} = 0$. The mechanical torque $T_m = 1.83$ kN·m (according to (44)) corresponds to $P_{set} = 500$ kW and $Q_{set} = 0$ VAr. We have $R = nR_s = 32.4$ Ω , $L = nL_s = 825$ mH, and $\phi = 82.87^\circ$.

The two equilibrium points with positive i_f values are:

$$\mathbf{z}_r^e = \begin{bmatrix} i_{dr}^e \\ \omega_g \\ \delta_r \\ i_{fr}^e \end{bmatrix} = \begin{bmatrix} -34.73 \\ -33.29 \\ 314.16 \\ 46.21^\circ \\ 1.67 \end{bmatrix}, \quad \mathbf{z}_l^e = \begin{bmatrix} i_{dl}^e \\ \omega_g \\ \delta_l \\ i_{fl}^e \end{bmatrix} = \begin{bmatrix} -368.81 \\ -6.01 \\ 314.16 \\ -90.93^\circ \\ 9.22 \end{bmatrix}.$$

Again, if we compute the active power P at the above two equilibrium points according to (21), we get that $P_r = 500$ kW at the stable equilibrium point (which is exactly P_{set}), and $P_l = -3.83$ MW at the unstable equilibrium point. In the following, we perform the same stability analysis of Example VI-A.

The equilibrium points \mathbf{z}_r^e corresponding to (P_r, \tilde{Q}) and \mathbf{z}_l^e corresponding to (P_l, \tilde{Q}) are shown in Fig. 10(b), on the smallest circle, which corresponds to $\tilde{T}_{m1} = 1.83$ kN·m, i.e., to $P_{set} = 500$ kW and $Q_{set} = 0$ VAr. For this circle, we get $I_{f1} = [1.21, 9.29]$ A. In the same figure, we also represent two other circles, corresponding to the equilibrium points of (13) for $\tilde{T}_{m2} = 18.18$ kN·m (i.e., $P_{set2} = 3000$ kW and $Q_{set2} = 200$ kVAr) and $\tilde{T}_{m3} = 45.19$ kN·m (i.e., $P_{set3} = 5400$ kW and $Q_{set3} = 400$ kVAr), for which, respectively, we get $I_{f2} = [7.28, 15.36]$ A and $I_{f3} = [13.12, 21.20]$ A. Also with these synchronverter values, it is clear from Fig. 10(b) that the equilibrium points \mathbf{x}_1^e are always stable for reasonable P_{set} and Q_{set} values. (Only for \tilde{T}_{m3} can we see a blue arc appearing.) This is confirmed by the light green area in Fig. 10(b), indicating the stability region of the fourth order model (13). Also in this case, the point M coincides with the centre of the green semidisk in Fig. 10(b), indicating the stability region of (13).

In Fig. 11(b) we show how the contours of the fifth order model (18) stability region vary for different values of \tilde{K} . We use the following values: $\tilde{K}_1 = 50$ kA·H, $\tilde{K}_2 = 135$ kA·H, and $\tilde{K}_3 = 300$ kA·H. Note that $\tilde{K} = \tilde{K}_2$ is the value corresponding to $K = 5$ kA, i.e., the one used above for the computation of \mathbf{z}_l^e and \mathbf{z}_r^e . Also in this case, it is not true that if $\tilde{K}_1 > \tilde{K}_2$, then $A(\tilde{K}_2) \subset A(\tilde{K}_1)$, as is clear from Fig. 11(b). Moreover, we observe, again, that for $\tilde{K} \rightarrow \infty$ the contours are approaching the green light area, indicating the intersection between the green sector from Fig. 9 and the stability region of (13).

VII. CONCLUSIONS

We have formulated a fifth order model for a grid-connected synchronverter, when the grid is considered to be an infinite bus. Conditions ensuring the existence of its equilibrium points

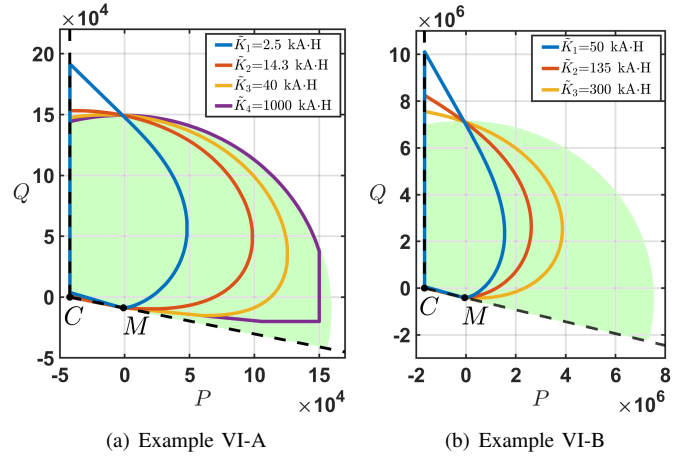


Fig. 11. The coloured shapes correspond to the contours of the stability region of the fifth order model (18), with the parameters from Example VI-A (Subfig. a) and from Example VI-B (Subfig. b), for different values of \tilde{K} . The points C, M are from Proposition 3.6, while the light green area indicates the intersection between the green sector from Fig. 9 and the maximal stability region of (13), with the parameters from Example VI-A (Subfig. a) and from Example VI-B (Subfig. b).

have been derived, and a novel geometrical representation has been introduced. This representation links the region of stability of the fourth order model from [20], [21], with the region of stability of our fifth order model. Moreover, using singular perturbation methods, we have derived sufficient conditions guaranteeing the existence of (local) exponentially stable equilibrium points for the fifth order model. Finally, the validity of our theoretical results has been proved using two numerical examples coming from the synchronverter literature.

REFERENCES

- [1] J. Alipoor, Y. Miura and T. Ise, "Distributed generation grid integration using virtual synchronous generator with adaptive virtual inertia," in *Proc. IEEE Energy Conversion Congress and Exposition (ECCE)*, Denver, CO, Sept. 2013, pp. 4546-4552.
- [2] R. Aouini, B. Marinescu, K. Ben Kilani and M. Elleuch, "Synchronverter-based emulation and control of HVDC transmission," *IEEE Trans. Power Systems*, vol. 31, 2015, pp. 278-286.
- [3] N. Barabanov, J. Schiffer, R. Ortega, and D. Efimov, "Conditions for almost global attractivity of a synchronous generator connected to an infinite bus," *IEEE Trans. on Automatic Control*, vol. 62, 2017, pp. 4905-4916.
- [4] H.-P. Beck and R. Hesse, "Virtual synchronous machine," in *Proc. 9th Int. Conf. on Electrical Power Quality and Utilisation (EPQU)*, Barcelona, Spain, 2007, pp. 1-6.
- [5] M. Blau and G. Weiss, "Synchronverters used for damping inter-area oscillations in two-area power systems," in *Int. Conf. on Renew. Energies and Power Quality (ICREPO)*, Salamanca, Spain, March 2018.
- [6] N. G. Bretas and L. F. C. Alberto, "Lyapunov function for power systems with transfer conductances: extension of the invariance principle," *IEEE Trans. on Power Systems*, vol. 18, no. 2, pp. 769-777, 2003.
- [7] S. Dong and Y.C. Chen, "Adjusting synchronverter dynamic response speed via damping correction loop," in *IEEE Trans. on Energy Conversion*, vol. 32, no. 2, pp. 608-619, 2017.
- [8] S. Dong, Y.-N. Chi and Y. Li, "Active voltage feedback control for hybrid multi-terminal HVDC system adopting improved synchronverters," *IEEE Trans. on Power Delivery*, vol. 31, pp. 445-455, 2016.
- [9] J. Driesen and K. Visscher, "Virtual synchronous generators," *IEEE Power and Energy Soc. General Meeting - Conversion and Delivery of Electrical Energy in the 21st Century*, Pittsburg, PA, July 2008, pp. 1-3.
- [10] P. Kundur, *Power System Stability and Control*, McGraw-Hill, New York, 1994.

- [11] Z. Kustanovich F. Reissner, S. Shivratri, G. Weiss, "The sensitivity of grid-connected synchronverters with respect to measurement errors," submitted in 2021.
- [12] Z. Kustanovich and G. Weiss, "Synchronverter based photovoltaic inverter," in *Proc. of ICSEE 2018*, Eilat, December 2018.
- [13] J. Liu, Y. Miura and T. Ise, "Fixed-parameter damping methods of virtual synchronous generator control using state feedback," *IEEE Access*, vol. 7, pp. 99177-99190, 2019.
- [14] P. Lorenzetti and G. Weiss, "PI control of stable nonlinear plants using projected dynamical systems theory," submitted in 2021.
- [15] P. Lorenzetti and G. Weiss, "Saturating PI control of stable nonlinear systems using singular perturbations," submitted in 2020, available on arXiv.
- [16] F. Mandrile, E. Carpaneto, R. Bojoi, "Grid-feeding inverter with simplified virtual synchronous compensator providing grid services and grid support," *IEEE Trans. on Industry Appl.*, vol. 57, pp. 559-569, 2021.
- [17] F. Mandrile, S. Musumeci, E. Carpaneto, R. Bojoi, T. Dragicevic and F. Blaabjerg, "State-space modeling techniques of emerging grid-connected converters," *Energies*, vol. 13, 2020.
- [18] A. A. Milani, M. T. A. Khan, A. Chakraborty, I. Husain, "Equilibrium Point Analysis and Power Sharing Methods for Distribution Systems Driven by Solid-State Transformers," *IEEE Transactions on Power Systems*, vol. 33, pp. 1473-1483, 2018.
- [19] O. Mo, S. D'Arco, J. A. Suul, "Evaluation of virtual synchronous machines with dynamic or quasi-stationary machine models," *IEEE Trans. Ind. Electronics*, vol. 64, pp. 5952-5962, 2017.
- [20] V. Natarajan and G. Weiss, "Almost global asymptotic stability of a grid-connected synchronous generator," *Math. of Control, Signals and Systems*, vol. 30, 2018.
- [21] V. Natarajan and G. Weiss, "Synchronverters with better stability due to virtual inductors, virtual capacitors and anti-windup," *IEEE Trans. on Industrial Electronics*, vol. 64, pp. 5994-6004, 2017.
- [22] Y. Ojo, J. Watson and I. Lestas, "A review of reduced-order models for microgrids: simplifications vs accuracy," available on arXiv, 2020.
- [23] J. Roldan-Perez, A. Rodriguez-Cabero and M. Prodanovic, "Design and analysis of virtual synchronous machines in inductive and resistive weak grids," *IEEE Trans. on Energy Conversion*, vol. 34, pp. 1818-1828, 2019.
- [24] P.W. Sauer and M.A. Pai, *Power Systems Dynamics and Stability*, Stipes Publishing, Champaign, IL, 1997.
- [25] J. Schiffer, R. Ortega, A. Astolfi, J. Raisch and T. Sezi, "Conditions for stability of droop-controlled inverter-based microgrids," *Automatica*, vol. 50, pp. 2457-2469, 2014.
- [26] Z. Shuai, W. Huang, Z. J. Shen, A. Luo and Z. Tian, "Active power oscillation and suppression techniques between two parallel synchronverters during load fluctuations," *IEEE Trans. on Power Electronics*, vol. 35, pp. 4127-4142, 2020.
- [27] A. Tayyebi, A. Anta, and F. Dörfler, "Hybrid angle control and almost global stability of grid-forming power converters," available on arXiv, 2020.
- [28] A. Tayyebi, D. Gross, A. Anta, F. Kupzog and F. Dörfler, "Frequency stability of synchronous machines and grid-forming power converters," *IEEE J. of Emerging and Selected Topics in Power Electronics*, vol. 8, pp. 1004-1018, 2020.
- [29] K. R. Vasudevan, V. K. Ramachandramurthy, T. S. Babu and A. Pouryekta, "Synchronverter: A comprehensive review of modifications, stability assessment, applications and future perspectives," *IEEE Access*, vol. 8, pp. 131565-131589, 2020.
- [30] P. Vorobev, P. Huang, M. Al Hosani, J. L. Kirtley and K. Turitsyn, "High-fidelity model order reduction for microgrids stability assessment" *IEEE Trans. on Power Systems*, vol. 33, no. 1, pp. 874-887, 2018.
- [31] H. Wu, X. Ruan, D. Yang, X. Chen, W. Zhao, Z. Lv and Q.C. Zhong, "Small-signal modeling and parameters design of virtual synchronous generators," in *IEEE Trans. Industrial Electronics*, vol. 63, pp. 4292-4303, 2016.
- [32] Y. Zhang and L. Xie, "A transient stability assessment framework in power electronic-interfaced distribution systems," *IEEE Trans. on Power Systems*, vol. 31, no. 6, pp. 5106-5114, 2016.
- [33] Q.-C. Zhong and T. Hornik, *Control of Power Inverters in Renewable Energy and Smart Grid Integration*, Wiley, Chichester, UK, 2013.
- [34] Q.-C. Zhong, G.C. Konstantopoulos, B. Ren and M. Krstic, "Improved synchronverters with bounded frequency and voltage for smart grid integration," *IEEE Trans. Smart Grid*, vol. 9, no. 2, pp. 786-796, 2018.
- [35] Q.-C. Zhong, P.-L. Nguyen, Z. Ma and W. Sheng, "Self-synchronized Synchronverters: Inverters without a dedicated synchronization units," *IEEE Trans. Power Electronics*, vol. 29, pp. 617-630, 2014.
- [36] Q.-C. Zhong and G. Weiss, "Static synchronous generators for distributed generation and renewable energy," in *Proc. IEEE PES Power Systems Conf. & Exhibition (PSCE)*, Washington, USA, March 2009.
- [37] Q.-C. Zhong and G. Weiss, "Synchronverters: Inverters that mimic synchronous generators," *IEEE Trans. Industr. Electronics*, vol. 58, pp. 1259-1267, 2011.

Pietro Lorenzetti is an Early Stage Researcher within the Marie Curie ITN project "ConFlex", who focuses his research on nonlinear control. Pietro has completed the bachelor degree in "Computer engineering and automation" at Universita Politecnica delle Marche, in Ancona. In 2015 he graduated with honors and he moved to Torino, where he enrolled the master degree in "Mechatronic Engineering" at Politecnico di Torino. In the same year, he also joined the double-degree program "Alta Scuola Politecnica", a highly selective joined program between Politecnico di Torino and Politecnico di Milano. In 2017 he graduated in both Politecnico di Milano and Politecnico di Torino, with honors. His research interests include nonlinear systems, nonlinear control, and power system stability.

Zeev Kustanovich received the B.Sc. degree from Ben Gurion University of the Negev, Beer Sheva, Israel, in 1997, and the M.Sc. degree from Technion, Haifa, Israel, in 2003 both in electrical engineering. Since 2003 he is Senior Electrical Engineer at the Israel Electricity Company. In 2018, he started his Ph.D. with the Power Electronics for Renewable Energy group in Tel Aviv University, Israel. His main research interests include power systems, renewable energy, control theory and applications to power system stability.

Shivprasad Shivratri received the B.Sc. degree in electrical and electronics engineering from Tel Aviv University, Israel, in 2018. In 2018, he started his M.Sc. with the Power Electronics for Renewable Energy group in Tel Aviv University and he graduated in May 2021. His research interests include control techniques in power systems and control theory.

George Weiss received the MEng degree in control engineering from the Polytechnic Institute of Bucharest, Romania, in 1981, and the Ph.D. degree in applied mathematics from the Weizmann Institute, Rehovot, Israel, in 1989. He was with Brown University, Providence, RI, Virginia Tech, Blacksburg, VA, Ben-Gurion University, Beer Sheva, Israel, the University of Exeter, U.K., and Imperial College London, U.K. His current research interests include distributed parameter systems, operator semigroups, passive and conservative systems (linear and nonlinear), power electronics, microgrids, repetitive control, sampled data systems, and wind-driven power generators. He is leading research projects for the European Commission and for the Israeli Ministry of Infrastructure, Energy and Water.